Evaluation of in-plane and out-of-plane crystallinities with residual amorphous phases for MgB_2 superconductor

Minoru Maeda[a], Jun Hyuk Choi[b], Dong Gun Lee[b], Akiyoshi Matsumoto[c], Gen Nishijima[c], Zhenan Jiang[d], Nicholas M. Strickland[d], Jung Ho Kim[e,*], Seyong Choi[a,*]

[a] *Department of Electrical Engineering and Kangwon High Magnetic Field Center, Institute of Quantum Convergence Technology, Kangwon National University, Gangwon 24341, Republic of Korea*

[b] *Sam Dong Co., Ltd., Daejeon 34027, Republic of Korea*

[c] *Superconducting System Group, Research Center for Energy and Environmental Materials (GREEN), National Institute for Materials Science (NIMS), Sengen, Tsukuba, Ibaraki 305-0047, Japan*

[d] *Paihau-Robinson Research Institute, Victoria University of Wellington, Wellington, Lower Hutt 5011, New Zealand*

[e] *Institute for Superconducting and Electronic Materials, Faculty of Engineering and Information Sciences, University of Wollongong, Squires Way, Innovation Campus, North Wollongong, New South Wales 2500, Australia*

*Corresponding authors: jhk@uow.edu.au (J.H. Kim); syc@kangwon.ac.kr (S. Choi)

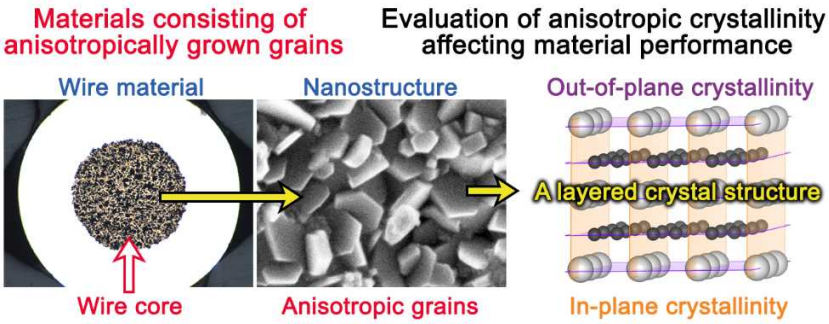

Abstract

In this study, we focus on in-plane and out-of-plane crystallinities of the MgB_2 superconductor. These two structural properties were evaluated in terms of peak broadening at lower angles in the X-ray diffraction. The angular behavior of the in-plane and out-of-plane peaks was used to compare it with the corresponding behavior estimated in the case of several crystallite sizes (that affect the in-field superconductivity of MgB_2). We propose that this comparison allows a simple evaluation to provide insight into the individual influences of in-plane and out-of-plane crystallinities on the in-field critical current density (without needing to calculate numerical values of crystallite sizes and lattice strains of fabricated MgB_2 materials). For this study, we used MgB_2 samples sintered at different temperatures. The sintering conditions affected not only the crystallinities but also the phase compositions. The behavior of the compositions, including amorphous phases, was also evaluated by using a quantitative analysis for X-ray diffraction results.

Keywords: Anisotropy, Disorder, MgB_2, X-ray diffraction

1. Introduction

Innovative applications, such as in the power grids across Europe and hybrid energy storage systems combined with hydrogen technologies [1–4], have been the focus of studies on MgB_2 materials (e.g., wires, tapes, and cables). The polycrystalline materials have been developed to have high performance of critical current density (J_c), especially in magnetic fields. To further enhance their transport performance, a profound understanding of the material crystallization/formation is indispensable. It is well known that the crystal structure of MgB_2 consists of magnesium (Mg) and boron (B) layers [5,6]. These two types of elemental layers are stacked alternately along the *c*-axis direction in the hexagonal lattice (Supplementary Fig. S1 in the Supporting Information). The layered crystal structure is very simple. The electronic structure responsible for the superconductivity is a complex structure, however, which contains quasi-two-dimensional (quasi-2D) σ bands parallel to the in-plane direction and nearly three-dimensional (3D) π bands

[7–10]. The dimensionally different bands do not interact strongly, and hence, two different superconducting energy gaps coexist [11–14]. The unique electronic structures form through in-plane covalent/metallic bonding (within the B layer) and delocalized metallic/ionic bonding (between the B-Mg-B layers) [7–10,15,16]. The different bonding states forming the layered crystal structure cause the anisotropies of structural disorder (where atomic/ionic arrangements are weakly or locally disordered compared with well-ordered arrangements), as reported in our previous study [17]. The disorder anisotropies can be evaluated by their in-plane and the out-of-plane crystallinities, which are characterized by their grain sizes, lattice strains, and crystallite sizes. These structural properties can affect the in-field performance of J_c and critical current (I_c) in terms of charge carrier scattering and/or vortex pinning. In particular, the out-of-plane strain and size have the potential to play an important role in the in-field transport properties in polycrystalline materials [17–19]. This is because the transport current moves through out-of-plane as well as in-plane interfaces between grains/crystallites. Elucidating the nature of the crystallinities in the two directions is thus of paramount importance in developing MgB_2 materials, which have a unique structure consisting of dimensionally different bands.

Evaluation of the crystallinity of MgB_2 materials has been performed so far by considering isotropic models in most cases [20–24], including our past study [25]. From the viewpoint of the anisotropy, we focused on and quantitatively evaluated the in-plane and the out-of-plane structural properties for disordered MgB_2 materials in our previous study [17]. The quantitative analytical method that we used is complicated, however, and includes a somewhat arbitrary (but reasonable) assumption that the strain and size distributions follow Gaussian and Lorentzian curves. Moreover, there has still been much less work on evaluation of the anisotropic crystallinity in MgB_2 materials. In this study, we introduce a qualitative and simple method for easy evaluation of the in-plane and the out-of-plane crystallinities. This evaluation approach also enables an indirect comparison of the crystallite sizes of fabricated samples with the coherence lengths for the σ and π bands in highly crystalline structures. This comparison is conducted through structural characterization in terms of peak broadening at lower angles in X-ray diffraction, and hence make it possible without needing to calculate numerical values of crystallite sizes and lattice strains

of the fabricated samples. The comparative analysis helps us to ascertain whether structural disorder (especially that caused by smaller crystallite sizes) influences the in-field superconductivity. In addition, the disordering of the material structure usually involves an increase in the content of amorphous phases, which were not considered in our previous study [17]. Accordingly, we have also performed a quantitative composition analysis to investigate the relationship between the phase content and the in-field transport performance in this study.

2. Experimental

The crystallinity of MgB_2 materials (focused on in this study) decreases as the sintering temperature is reduced. This change in crystallinity is universal and occurs whether the material is in bulk, wire, or powder form. To investigate the structural and material properties, including crystallinity, both MgB_2 wire and powder samples were used. Different sintering temperatures for the samples were also employed to change their crystallinity. The fabrication methods are described below. The wire and powder samples were prepared through *in situ* processes using iron (Fe) tubes, Mg powder (spherical and elliptical shapes, an average size of 16 μm, Hana AMT), amorphous B powder (purity of 98.5 %, median size of 288 nm [26], Pavezyum), and pyrene ($C_{16}H_{10}$) powder (purity of 98%, Sigma-Aldrich). The hydrocarbon material was used for carbon doping to enhance the in-field J_c performance [27]. The doping level, x, reflecting a molar ratio of $1:2-x:x/16$ between Mg, B, and $C_{16}H_{10}$, was set at 0.10. The three powders of Mg, B, and $C_{16}H_{10}$ were mechanically mixed in a tumbler mixer. The mechanical processing was performed at a rotation rate of 40 rpm for 30 minutes in a glove box with an argon (Ar) atmosphere. The mechanically mixed powder was used to fabricate both MgB_2 powder and wire samples. The rest of the fabrication process for the wire samples is explained below. The mechanically mixed powder was poured into Fe tubes in air. The filled tubes were deformed into round wires 1.0 mm in diameter by using a draw bench. The mechanically deformed wires were sintered to form the MgB_2 phase in their cores. The sintering processes were carried out in a tube furnace with flowing Ar gas at 100 standard cubic centimeters per minute (sccm). The sintering conditions of the wires were 600 ºC, 625 ºC, 640 ºC, 660 ºC, and 695 ºC for 8 h. These sintered wires were

used as MgB_2 wire samples in this study. The weights of each wire sample remained almost the same before and after the sintering. The lengths and the core sizes of each fabricated wire were approximately 100.6 cm and 0.00203 cm^2, respectively. The weight of the mixed powder used for each wire fabrication was 0.3 g. From the above data, the core density of each sample was estimated to be 1.5 (± 0.1) g/cm^3, which is approximately 58% of the theoretical density of 2.6 g/cm^3 for MgB_2.

The rest of the fabrication process for MgB_2 powder samples is explained below. The mechanically mixed powder mentioned above was put into iron tubes in a glove box with an Ar atmosphere. Both ends of the tubes were then pressed with a bench vice. The enclosed tubes were placed in a tube furnace with flowing Ar gas at 100 sccm. The gas-flow furnace was operated under the same sintering conditions that were used for the wire samples. After the sintering processes, the powder samples were extracted from the enclosed tubes. The extracted powders were used as MgB_2 powder samples in this study. These fabrication methods for the powder and wire samples are the same as those shown in our previous study [17]. Further information can be seen in the previous article, which describes the details of the mixing conditions (e.g., the total amount of raw powders, the ball-to-powder mass ratio, the mixing motion, and the materials of mixing tools).

Measurement methods described below were used to examine structural and superconducting properties of the wire samples. The grain structures of the samples were investigated by field-emission scanning electron microscopy (FE-SEM, FEI, Apreo S HiVac). Elemental analysis for the samples was performed by using an energy dispersive spectroscopy (EDS) detector (Burker, XFlash 6-100). Void structures of the samples were observed by optical microscopy (OM) (Zeiss, Axio Observer). Transport critical currents of the samples were measured at a temperature of 4.2 K under liquid helium (He) immersion cooling. The transport properties at 20 K were also recorded using a He gas-flow cryostat. The transport currents at 4.2 K and 20 K were supplied by a higher current power supply (Agilent, 6680A) and a lower current power supply (Hewlett Packard, 6671A), respectively. By using the former supply and the latter supply, the applied transport currents for the samples were increased from 0 A up to a maximum of 411 A and from 0 A up to a maximum of 7 A, respectively. These transport measurements of the samples were conducted by the

standard four-probe method and under an applied field of 5 T. The electric field criterion to determine the critical currents was set at 1.0 μV/cm. The transport J_c for each sample was determined by taking the ratio of the critical current to the cross-sectional area of the wire core for the corresponding sample.

The MgB_2 powder samples were investigated by measurement methods described below. X-ray diffraction (XRD) patterns of the samples were collected over a wide range of angles up to 145º. The obtained patterns were analyzed through Rietveld refinement. The structural analysis was performed using the VESTA program [28] and the RIETAN-FP program [29]. Through this analysis, calculated XRD patterns fitted to the experimental data were obtained. The broadening of the XRD peaks caused by lower crystallinity was evaluated in terms of integral breadth (which is defined by dividing the integrated intensity of the diffraction peak by its height). Amorphous phases of the samples were quantitatively evaluated by XRD analysis through the following simple equation [29–35]:

$$w_a = 1 - \sum_p w_p, \qquad (1)$$

where w_a and w_p are the weight fractions of the amorphous phases and each crystalline phase, respectively. As can be seen on the right side of the above equation, the quantitative evaluation requires the total quantity of weight fractions for all the crystallized compositions present in a sample. The individual contents of the crystalline phases can be estimated through Rietveld refinement of the XRD patterns, including an additive that serves as an internal standard material [29–31]. For this purpose, silicon (Si) powder (National Institute of Standards and Technology (NIST), 640e) was mixed with our powder samples sintered at different temperatures (as mentioned above). The mixtures including the standard material were scanned during the XRD measurements. The obtained XRD patterns were also analyzed using Rietveld refinement through the VESTA program [28] and the RIETAN-FP program [29] for the quantitative evaluation of the phase contents mentioned above.

3. Results and discussion

Fig. 1 shows the XRD patterns of the powder samples. The diffraction patterns were found to include

highly intense and sharp peaks (denoted by the symbols of upright triangles). This peak behavior arises from the Si phase, which was added for the quantitative XRD analysis, as explained in section 2. The Si phase was identified using a diffraction data set provided by NIST, which produced the Si powder. Apart from this additional phase, the crystalline compositions present in the samples were identified using the XRD patterns. The phase identification revealed that the samples consisted of MgB_2 phase with minor impurities of MgO and unreacted Mg, as briefly mentioned in our previous study [17]. The identification of these phases was performed using powder diffraction files (PDF) of MgB_2 (PDF#38-1369), MgO (PDF#004-0829), and Mg (PDF#35-0821). Here, the details of the crystalline impurity phases are discussed. Diffraction peaks of the MgO phase in the XRD patterns were observed at around 62º, as denoted by the arrow in Fig. 1. The peak intensities were very weak and remained almost constant despite the sintering at different temperatures. In contrast to this independent behavior, the diffraction peaks of the unreacted Mg phase (denoted by the inverted triangles) became stronger when the sintering temperature decreased. The upturn in the peak intensity may also be indicative of an increase in the content of unreacted amorphous B particles, which cannot be detected as distinct diffraction peaks due to their lack of long-range order. The increase in the amorphous content may contribute to elevation of the background intensity in XRD patterns, as shown in Supplementary Fig. S2.

The observed XRD patterns of the powder samples were analyzed by Rietveld refinement. The calculation results are plotted as white curves in Fig. 1. Their white plot lines can be seen on the black and red curves in the figure. The calculated patterns were found to be well fitted to the experimental data. The fitted results provided quantitative information on the sample compositions, as shown in Fig. 2. The compositional structures were characterized in terms of crystalline and amorphous phases. The latter content can be affected by the residual B phase, as explained in the previous paragraph. The weight fraction of the amorphous phases exhibited an exponential-like rise with decreasing sintering temperature (see Fig. 2). A similar trend was also observed for the weight fraction of the unreacted Mg phase. These upward changes in the remaining impurities may directly influence the formation of the MgB_2 phase in the samples. In fact, the MgB_2 phase content logarithmically decreased due to the correlation with their residual effects, which

were enhanced by reducing the sintering temperature. In contrast to the large change of these phase contents mentioned above, the content of the MgO phase remained almost intact. Accordingly, the metal oxide is chemically stable against the reaction temperatures for MgB_2 materials, unlike the other phases. The stable oxide, even when functioning as pinning centers of vortices or serving as current-blocking obstacles, does not contribute to any significant change in the observed J_c performance for the wire samples, which were sintered at different temperatures, as explained later.

The transport J_c performance of MgB_2 materials may depend not only on the impurity phases, but also on the crystallinity, including the structural behavior of grain/crystallite boundaries. The latter properties can be characterized by lattice strain and crystallite size. The structural states can be evaluated by a simple XRD analysis, as described in the following. It is well known that an observed XRD pattern is determined by contributions from the lattice strain, crystallite size, and instrumental conditions. The latter contributions to the broadening of XRD peaks can be removed through utilization of a pseudo-Voigt function, which linearly combines the Gaussian and the Lorentzian functions [36]. This mathematical model is often employed to evaluate the integral breadth (β_{obs}) for the observed diffraction peaks through Rietveld refinement. The refinement results of the diffraction peaks used in this study are shown in Supplementary Fig. S3. In our previous study [17], the diffraction-angle dependence of β_{obs} was employed to graphically display different anisotropic effects of more- and less-disordered MgB_2 structures. The β_{obs} focused on here is characterized by the pseudo-Voigt distribution, which is nearly identical to the peak shapes of Voigt functions [37]. The Voigt model consists of a convolution of the Gaussian and Lorentzian functions. The integral breadths ($\beta_{G,obs}$ and $\beta_{L,obs}$) of the two constituent components can be estimated using the β_{obs} values [36]. The estimated breadths include the two instrumental contributions ($\beta_{G,inst}$ and $\beta_{L,inst}$) in terms of the Gaussian and the Lorentzian distributions. The instrumental effects on $\beta_{G,obs}$ and $\beta_{L,obs}$ behavior can be excluded using the following relations that hold because of the convolution theorem.

$$\left(\beta_{\mathrm{G,obs}}\right)^2 = \left(\beta_{\mathrm{G,sample}}\right)^2 + \left(\beta_{\mathrm{G,inst}}\right)^2 \qquad (2)$$

$$\beta_{\mathrm{L,obs}} = \beta_{\mathrm{L,sample}} + \beta_{\mathrm{L,inst}} \qquad (3)$$

The excluded values ($\beta_{G,sample}$ and $\beta_{L,sample}$) can be used to obtain the intrinsic integral breadth (β_{sample}), which is determined by the structural properties of the samples [36]. To estimate the β_{sample} values using the above-mentioned analysis, the calculated values obtained in this study are shown in Supplementary Tables S1–S5 in the Supporting Information.

Fig. 3(a) shows the β_{sample} values of the MgB_2 peaks indexed as 00*l*, which arise from the out-of-plane structural states formed at different temperatures. In the formed structures, the lattice strain and crystallite size can affect the β_{sample} behavior, but only the size effect strongly contributes to the peak broadening at lower diffraction angles. The size broadening β_{size} for integral breadth on a 2θ scale can be expressed by the following equation [38]:

$$\beta_{\text{size}} = \frac{K\lambda}{D\cos\theta} \ , \quad (4)$$

where λ represents the X-ray wavelength used for the XRD measurement and D represents the volume-weighted mean thickness perpendicular to the diffraction planes when the Scherrer constant K is set to 1.0. The thickness is the mean size of coherently diffracting domains within grains, which is why D is commonly identified as the crystallite size. Referring to the crystallite boundary, D is also interpreted as the mean periodic distance between boundary defects. Such defects characterized by D decrease the mean free path for charge carriers and can reduce the coherence length (e.g., in terms of the Pippard model). 35 nm and 50 nm were selected as D values for comparative evaluation. The size effects are plotted in Fig. 3(a), as denoted by blue and purple dashed lines. The selected sizes are almost the same as the out-of-plane coherence lengths for the π bands, which have been experimentally reported or can theoretically be estimated for clean MgB_2 samples reported in the literature [39,40] (see the lengths (ξ_{π}^{c} and $\xi_{0,\pi}^{c}$) listed in Supplementary Tables S6 and S7 of the Supporting Information). Here, the clean samples are defined as having well-ordered crystal structures without significant distortion or many defects. The clean structures can be regarded as a standard for comparison to evaluate how effective the crystallite sizes of our samples are in improving the in-field superconductivity. For example, when the out-of-plane structures were formed at the sintering temperatures of 640 ºC and above, the β_{sample} values at lower diffraction angles approximately match the β_{size} values

estimated in the simulated cases of 35 nm and 50 nm (Fig. 3(a)). This implies that the crystallite sizes, corresponding to the mean periodic distances along the out-of-plane direction, are nearly comparable to the simulated lengths (35 nm and 50 nm). The mean distances between the crystallite boundaries are not very different from the coherence lengths for the π bands in the clean samples. In addition, the out-of-plane crystallite sizes became much shorter in the samples sintered at 600 ºC and 625 ºC, as indicated by significant increases in the β_{sample} values at lower diffraction angles (denoted by the red arrow in Fig. 3(a)). Such highly disordered structures (which also include the lattice strain) compared to clean samples can be identified as effective states for the reduction of the out-of-plane coherence length, which may contribute to improvement of the in-field superconductivity for the π bands. This effect is important for polycrystalline MgB_2 materials, if the in-field supercurrent along the *c*-axis direction affects the global critical current performance.

The above comparative method focusing on the crystallite size can be applied to evaluation of the in-plane structures, which can be characterized by the β_{sample} behavior of the MgB_2 peaks indexed as $hk0$ ($h \neq 0$). Fig. 3(b) shows the β_{sample} behavior for the samples sintered at different temperatures. The size effects of 10 nm, 40 nm, and 50 nm are also plotted in the figure. The former and the latter two sizes selected here almost correspond to the in-plane coherence lengths for the σ and the π bands, respectively, in the clean samples that are compared as references [40–42] (see the lengths (ξ_{σ}^{ab}, $\xi_{0,\sigma}^{ab}$, ξ_{π}^{ab}, and $\xi_{0,\pi}^{ab}$) listed in Supplementary Tables S6 and S7 of the Supporting Information). It turns out that the β_{size} values obtained in the simulated cases of 40 nm and 50 nm are likely to fall below or approach the lower-angle results of the β_{sample} behaviors for the samples (Fig. 3(b)). Since the simulated sizes are set to comparable distances of the coherence lengths for the π bands in clean samples, the crystallite sizes of our samples can be determined to be small enough to enhance the in-field superconductivity for the π bands. Compared to the coherence length for the σ bands in clean samples, however, the in-plane crystallite sizes were too large. This is apparent from the huge gap between the β_{sample} curves for the samples and the β_{size} curve estimated in the simulated case of 10 nm, as denoted by the black arrow in Fig. 3(b). From the size relation revealed by the comparative evaluation, it is concluded that the coherence length for the σ bands is not strongly impacted

by the relatively large crystallite size alone. Since long-range ordering of the crystallized structure is disordered not only by the crystallite boundaries, but also by the lattice strain, the latter rather than the former can be recognized as a determining factor that can give rise to the improved performance observed in the in-field J_c properties of our wire samples, as described later. Thus, the above comparative method helps to clarify whether the structural states of crystallites are effective in improving the in-field superconductivity for multi-band MgB_2 materials.

The in-field transport performance can be influenced by grain size as well as crystallite size and lattice strain. The grain structures of the wire samples sintered at 600 ºC, 625 ºC, and 695 ºC were evaluated by FE-SEM observations. Fig. 4(a–c) shows the observed results for the wire cores. It was found that hexagonal or hexagonal-like grains were formed in the core structures. The crystal grains can be characterized by their hexagonal size and height (Fig. 4(d)). The former and latter are presumed to correspond to the grain sizes along the in-plane and the out-of-plane directions for the MgB_2 phase, respectively, which has a hexagonal lattice in its layered crystal structure (Supplementary Fig. S1 in the Supporting Information). The observed crystal grains grew anisotropically, as can be seen from the apparent differences between the in-plane size (the hexagonal size) and the out-of-plane size (the height) (Fig. 4(a–c)). The anisotropic growth mechanism and the influence on grain-boundary pinning were explained in our previous study [17]. Here, several hexagonal or hexagonal-like grains with small heights were evaluated by FE-SEM observations. Interestingly, the heights outlined by the light-blue squares in Fig. 4(a, b) were comparable to or below the size ranges of 35 nm and 50 nm, which approximately equate to the out-of-plane coherence lengths for the π bands in clean samples (Supplementary Tables S6 and S7). Such short distances between grain boundaries (in addition to the out-of-plane crystallite size and lattice strain) may contribute to improving the in-field performance of the π-band superconductivity.

Besides the potential positive effect, different grains associated with negative contributions are also mentioned here. Such grain structures were found especially in local areas of the wire core sintered at 600 ºC. A secondary electron image of the local structures is shown in Fig. 4(e). The observed result revealed that several grains were not highly crystalline, as denoted by the yellow arrow in the figure. To investigate

the elemental composition, two positions, Spot 1 and Spot 2, in the grain structure were targeted. EDS spectra collected from Spot 1 and Spot 2 are shown in Fig. 4(f) and (g), respectively. The spectral patterns were found to include four peaks for elements of B, C, O, and Mg. The elemental compositions in atomic percent (estimated from the spectral patterns) are listed in the insert tables of Fig. 4(f) and (g). Interestingly, a high concentration for the element B was detected especially for the grains at and around Spot 1. The atomic ratio of B/Mg is approximately 8.6, which is much higher than the initial ratio of 1.9 (=1.9/1.0) used for the sample fabrication. In addition, as can be verified from Fig. 4(i–k), the atomic ratios for Spot 3 and Spot 4 in hexagonal or hexagonal-like grains are 2.1 and 1.7, which is much lower than that for Spot 1. The grain morphologies at and around Spot 1 are rather close to spherical and spherical-like shapes of amorphous B particles, as can be seen in Fig. 4(h). These similar shapes, in connection with the EDS results, imply that the spherical and spherical-like grains in Fig. 4(e) are unreacted or partly reacted B particles. Such residues from the raw powder decrease the formation of the superconducting phase in polycrystalline MgB_2 materials, as explained in connection with the XRD results. In addition, the small grains, like the residues, were not well connected in the core structure (Fig. 4(e)). The low-connectivity regions, likely due to locally incomplete reactions, reduce the effective cross-sectional area for the transport current in the wire core, even if the grains consist of only the MgB_2 phase.

Apart from the grain characteristics, voids limiting the transport performance were evaluated for the wire samples. The void evaluation was carried out using optical microscopy. Fig. 5(a–f) shows optical images of cross-sectional areas of the wire samples. As can be seen in Fig. 5(a), the cross-sectional structure consists of two main regions: an Fe sheath and a wire core. The latter region at higher magnification for each sample is shown in Fig. 5(b–f). The observation images were found to include areas with a metallic luster like gold and dark areas such as black. The former and the latter indicate relatively dense areas and large voids, respectively. The red squares shown in Fig 5(b–f) are also provided as a guide to identifying voids in the observation images. It was observed that the wire cores include numerous voids. The void structure is a typical feature of MgB_2 wires in the case of *in situ* fabrication [43]. The void formation is caused by Mg diffusion into areas of B powder to form the MgB_2 phase during the sintering process. As can

be seen in Fig. 5(b–f), the void morphologies did not drastically change between the wire samples sintered at 600–695 ºC (unlike the case of a clear reduction in the number of large voids [44]). Despite the observed similar structures, however, the transport J_c at 4.2 K in a magnetic field of 5 T was approximately doubled by reducing the sintering temperature, as shown in Fig. 6. The reason for using the field of 5 T as our measurement condition is that the J_c performance (especially at 20 K) becomes severely degraded when the crystallinity of the MgB_2 phase increases [45]. An enhanced effect on the in-field J_c due to a lower temperature for the sintering was also seen in the measurement results even at 20 K and 5 T (Fig. 6). It was obvious that these transport properties are quite sensitive to the sintering conditions, which diminish the crystallinity of the MgB_2 phase, for example in terms of crystallite size, as indicated by the β_{sample} behaviors at lower diffraction angles (Fig. 3). The disordered structures are most likely responsible for the enhanced performance of the in-field superconductivity, as explained from the viewpoint of the mechanism in the above paragraphs. It should also be noted that although a positive effect on the in-field J_c at 5 T was obtained by the low-temperature sintering, the crystallization process involves increases in the contents of partially reacted or unreacted phases (Figs. 2 and 4). Thus, better control of the residues while forming smaller grains/crystallites is thought to be one of the next issues that should be addressed in further development of MgB_2 materials.

4. Conclusions

In this study, we have concentrated on the analysis and characterization of MgB_2 materials with respect to their crystallinity and phase compositions. The latter properties were quantified, considering both crystalline and amorphous phases. The quantitative results revealed a logarithmic decrease in the content of the MgB_2 phase when the sintering temperature was reduced. However, the sintering effect with the carbon doping also diminished the crystallinity of the boride phase. These structural changes may ultimately lead to enhancement of the in-field J_c properties at 4.2 K and 20 K for MgB_2 materials. The material structures responsible for the enhanced performance were also evaluated by our proposed method, in which clean samples having high crystallinities are used for comparison. This comparative approach enabled simple and

qualitative characterization of the in-plane and out-of-plane disorder/crystallinity in the layered crystal structure of MgB_2. The structural characterization helped to determine whether the disordered states are effective for enhancing the in-field critical current performance of MgB_2 materials that have unique electronic states caused by dimensionally different bands. Therefore, for further understanding and development of the multi-band materials, the comparative method presented in this study is useful as an analytical option.

Acknowledgements

This work was performed by Support program for Kangwon High Magnetic Field Research Center through the Gangwon Technopark(GWTP) funded by Gangwon Province. This work was also supported by National R&D Program through the National Research Foundation of Korea (NRF) funded by Ministry of Science and ICT (2022M319A1076881).

Figure captions

Fig.1. XRD patterns of mixtures of the MgB_2 powder samples and the Si powder. The latter powder is used as an internal standard material for XRD analyses. The former powders were sintered at 600 ºC, 625 ºC, 640 ºC, 660 ºC, and 695 ºC for 8 hours. The lines of red and black plots are the observed XRD patterns of the mixtures. The thin gray lines, overlapping the red and black lines, are the calculated patterns obtained by Rietveld refinement. The Miller indices (*hkl* = 100, 101, 002, 110, and 102) denote peaks of the MgB_2 phase. The upright triangles, inverted triangles, and arrow denote the Si phase, Mg phase, and MgO phase, respectively.

Fig. 2. The relationship between sintering temperature of the MgB_2 powder samples and their phase compositions. (a) Temperature dependence of the weight fraction of the MgB_2 phase. (b) Corresponding dependences in the case of impurity phases. Impurities are the amorphous phases, unreacted Mg phase, and MgO phase. All weight fractions plotted in this figure were evaluated using Rietveld refinement and Equation (1).

Fig. 3. Structural behavior characterized by β_{sample} of the MgB_2 peaks in the XRD patterns for the MgB_2 powder samples. (a) The relationship between diffraction angles (two theta) and β_{sample} of the out-of-plane peaks indexed as 001, 002, 003, and 004 in *hkl*. (b) The corresponding relationship in the case of the in-plane peaks indexed as 100, 110, 200, 210, and 300 in *hkl*. The β_{sample} values plotted in these figures were evaluated by removing the contribution of instrumental conditions from the β_{obs} values of the MgB_2 powder samples, which were sintered at 600 ºC, 625 ºC, 640 ºC, 660 ºC, and 695 ºC for 8 hours. The green, blue, orange, and purple dashed lines plotted in these figures are β_{sample} curves when crystallite sizes are 10 nm, 35 nm, 40 nm, and 50 nm, respectively. These calculated curves (shown by the dashed lines) were obtained using Equation (4) and used for comparison with the β_{sample} curves of the MgB_2 powder samples at lower diffraction angles (where only the effect of the crystallite size strongly contributes to the β_{sample} values). The red arrow denotes that when the sintering temperature was 600 ºC or 625 ºC, the β_{sample} values of the out-of-plane peaks at lower diffraction angles became much higher than those in the case of the crystallite sizes of 35 nm and 50 nm. The black arrow denotes that the β_{sample} values of the in-plane peaks at lower diffraction angles were much smaller than those in the case of the crystallite size of 10 nm.

Fig. 4. (a–c) Secondary electron images of grain structures inside the cores of the wire samples sintered at (a) 600 ºC, (b) 625 ºC, and (c) 695 ºC. Grains observed in these areas have the shape of hexagonal or hexagonal-like prisms. The light-blue squares denote the sides of the hexagonal or hexagonal-like prisms. (d) Schematic depiction of the height and hexagonal size of a crystal grain shaped with a hexagonal structure. (e) A secondary electron image of a low-connectivity region in the core of the wire sample sintered at 600 ºC. This region includes spherical and spherical-like grains denoted by the yellow arrow. The positions shown by Spot 1 and Spot 2 were targeted for EDS microanalysis. (f, g) EDS spectra collected from Spot 1 and Spot 2. (h) A secondary electron image of boron powder used as a raw material for the fabrication of the wire samples. (i) A secondary electron image of a well-connected region in the core of the wire sample sintered at 600 ºC. This region includes hexagonal-like or hexagonal grains. The positions shown by Spot 3 and Spot 4 were targeted for EDS microanalysis. (j, k) EDS spectra collected from Spot 3 and Spot 4. The images (a–c) and (h) have the same scale length of 100 nm. The images (e) and (i) have the same scale

length of 500 nm. The tables inserted in Fig. 4(f), (g), (j), and (k) show the analytical results of elemental compositions obtained from the EDS spectra for Spot 1, Spot 2, Spot 3, and Spot 4, respectively. The elements detected from the EDS spectra were Mg, B, C, and O.

Fig. 5. (a–f) Optical images of cross-sectional areas of the wire samples sintered at (a, b) 600 ºC, (c) 625 ºC, (d) 640 ºC, (e) 660 ºC, and (f) 695 ºC. The cross-sectional areas were polished before the optical observations. The image (a) has a scale bar of 200 μm (denoted by the white line) and shows two main regions: an Fe sheath and a wire core. The latter region is further magnified. The observation results at a high magnification for all the wire samples are shown in the images (b–f). Areas characterized by a gold-colored metallic luster denote dense regions. Dark areas, denoted by the red squares, are voids. The images (b–f) were collected at the same magnification. This means that these images have the same scale length of 50 μm, as shown by the white lines.

Fig. 6. Transport J_c at 5 T as a function of sintering temperature for the wire samples. The measurement temperatures were 4.2 K and 20 K. The measurement at the latter temperature was conducted by using a He gas-flow cryostat. The former temperature was maintained using liquid He immersion cooling.

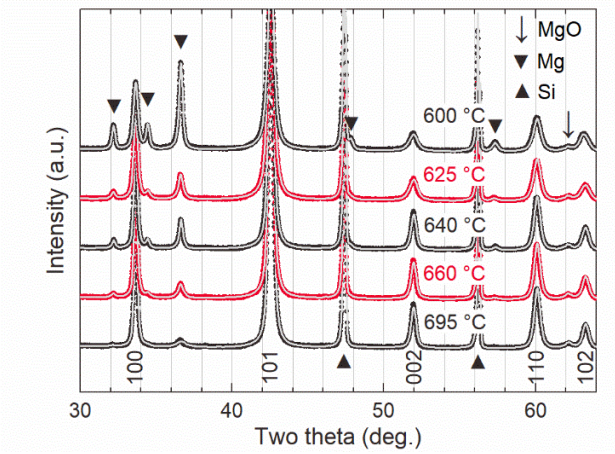

Fig. 1.

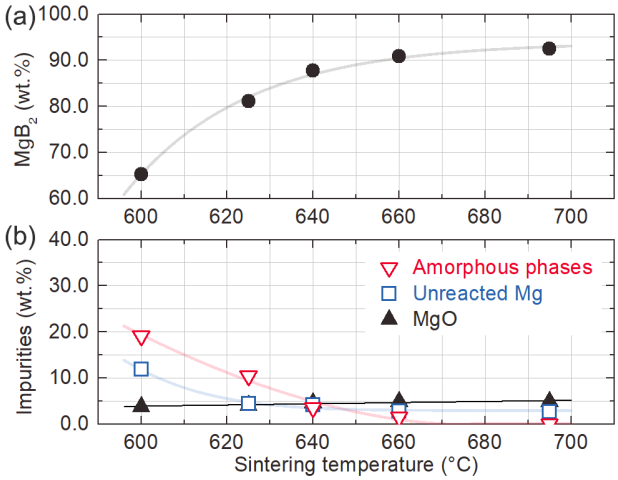
(a)
100.0
90.0
80.0
70.0
60.0
MgB2 (wt.%)
600
620
640
660
680
700
(b)
40.0
30.0
20.0
10.0
0.0
Impurities (wt.%)
Amorphous phases
Unreacted Mg
MgO
600
620
640
660
680
700
Sintering temperature (°C)

Fig. 2.

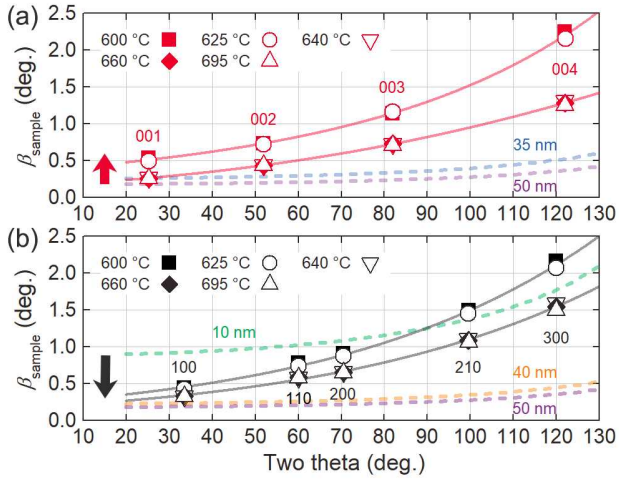
(a)
2.5
2.0
1.5
1.0
0.5
0.0
βsample (deg.)
600 °C
625 °C
640 °C
660 °C
695 °C
001
002
003
004
35 nm
50 nm
10
20
30
40
50
60
70
80
90
100
110
120
130
(b)
2.5
2.0
1.5
1.0
0.5
0.0
βsample (deg.)
600 °C
625 °C
640 °C
660 °C
695 °C
10 nm
100
110
200
210
300
40 nm
50 nm
10
20
30
40
50
60
70
80
90
100
110
120
130
Two theta (deg.)

Fig. 3.

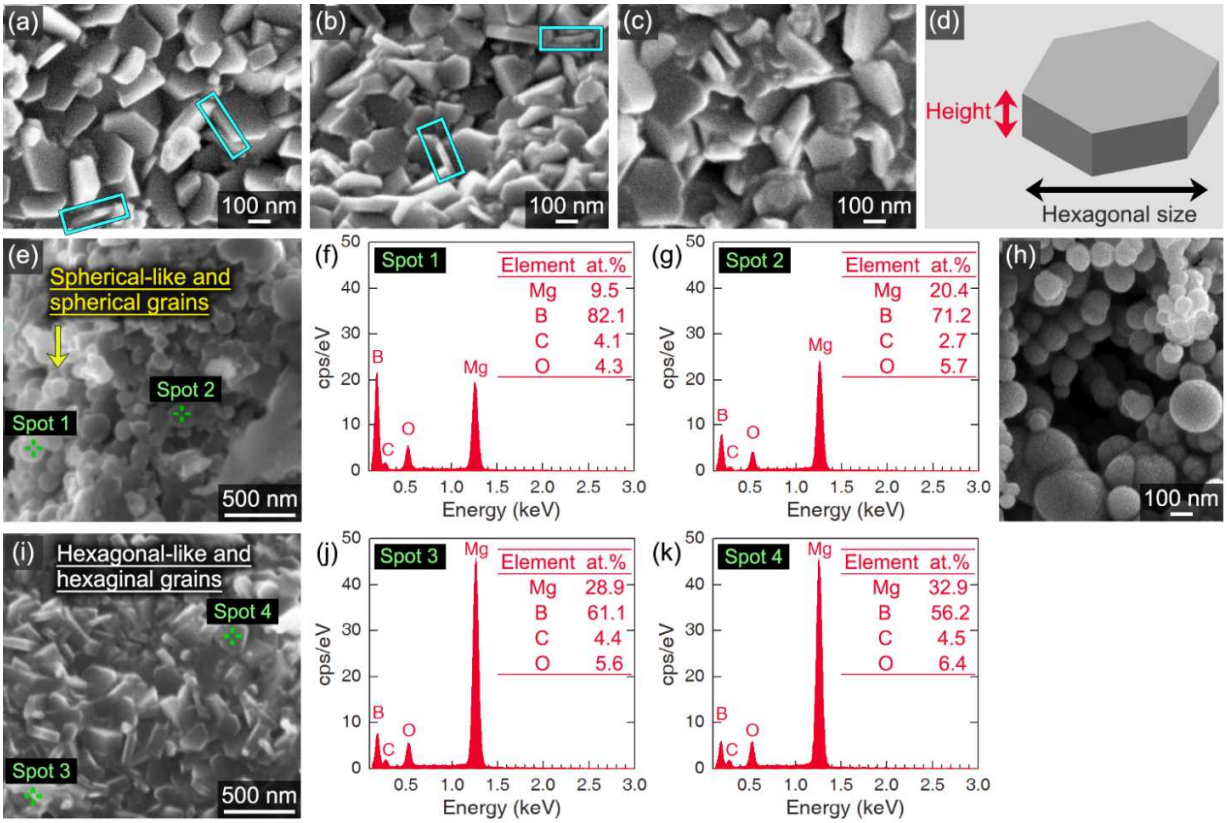
(a)
100 nm
(b)
100 nm
(c)
100 nm
(d)
Height
Hexagonal size
(e)
Spherical-like and spherical grains
Spot 1
Spot 2
500 nm
(f)
Spot 1
Element at.%
Mg 9.5
B 82.1
C 4.1
O 4.3
cps/eV
Energy (keV)
(g)
Spot 2
Element at.%
Mg 20.4
B 71.2
C 2.7
O 5.7
(h)
100 nm
(i)
Hexagonal-like and hexaginal grains
Spot 3
Spot 4
500 nm
(j)
Spot 3
Element at.%
Mg 28.9
B 61.1
C 4.4
O 5.6
(k)
Spot 4
Element at.%
Mg 32.9
B 56.2
C 4.5
O 6.4

Fig. 4.

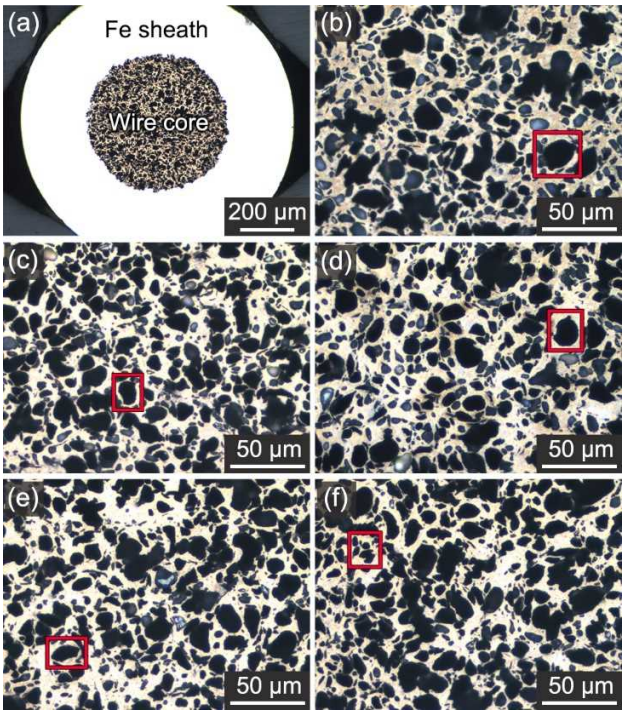
(a)
Fe sheath
Wire core
200 μm
(b)
50 μm
(c)
50 μm
(d)
50 μm
(e)
50 μm
(f)
50 μm

Fig. 5.

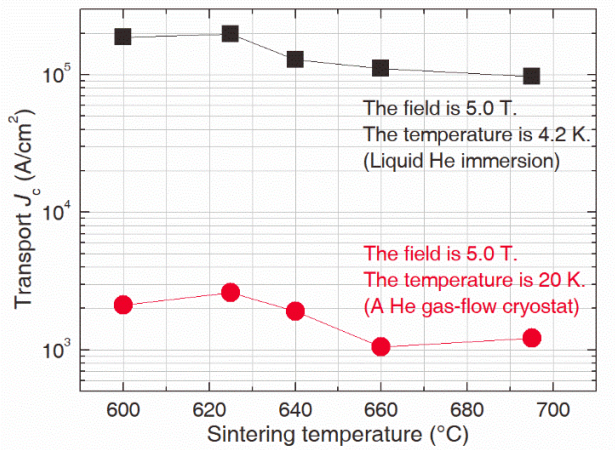
Transport J_c (A/cm^2)
10^5
10^4
10^3
The field is 5.0 T.
The temperature is 4.2 K.
(Liquid He immersion)
The field is 5.0 T.
The temperature is 20 K.
(A He gas-flow cryostat)
600
620
640
660
680
700
Sintering temperature (°C)

Fig. 6.

References

[1] A. Ballarino, C.E. Bruzek, N. Dittmar, S. Giannelli, W. Goldacker, G. Grasso, F. Grilli, C. Haberstroh, S. Holé, F. Lesur, A. Marian, J.M. Martínez-Val, L. Martini, C. Rubbia, D. Salmieri, F. Schmidt, M. Tropeano, The BEST PATHS Project on MgB_2 Superconducting Cables for Very High Power Transmission, IEEE Trans. Appl. Supercond. 26 (2016) 5401705.

[2] S. Klöppel, A. Marian, C. Haberstroh, C. Bruzek, Thermo-hydraulic and economic aspects of long-length high-power MgB_2 superconducting cables, Cryogenics 113 (2021) 103211.

[3] T. Hamajima, H. Amata, T. Iwasaki, N. Atomura, M. Tsuda, D. Miyagi, T. Shintomi, Y. Makida, T. Takano, K. Munakata, M. Kajiwara, Application of SMES and fuel cell system combined with liquid hydrogen vehicle station to renewable energy control, IEEE Trans. Appl. Supercond. 22 (2012) 5701704.

[4] T. Yagai, S. Mizuno, T. Okubo, S. Mizuochi, M. Kamibayashi, M. Jinbo, T. Takao, N. Hirano, Y. Makida, T. Shintomi, T. Komagome, K. Tsukada, T. Onji, Y. Arai, A. Ishihara, M. Tomita, D. Miyagi, M. Tsuda, T. Hamajima, Development of design for large scale conductors and coils using MgB_2 for Superconducting Magnetic Energy Storage Device, Cryogenics 96 (2018) 75-82.

[5] M.E. Jones, R.E. Marsh, The Preparation and Structure of Magnesium Boride, MgB_2, J. Am. Chem. Soc. 76 (1954) 1434-1436.

[6] J. Nagamatsu, N. Nakagawa, T. Muranaka, Y. Zenitani, J. Akimitsu, Superconductivity at 39 K in magnesium diboride, Nature 410 (2001) 63-64.

[7] J. Kortus, I.I. Mazin, K.D. Belashchenko, V.P. Antropov, L.L. Boyer, Superconductivity of Metallic Boron in MgB_2, Phys. Rev. Lett. 86 (2001) 4656-4659.

[8] J.M. An, W.E. Pickett, Superconductivity of MgB_2: Covalent Bonds Driven Metallic, Phys. Rev. Lett. 86 (2001) 4366-4399.

[9] K.D. Belashchenko, M. van Schilfgaarde, V.P. Antropov, Coexistence of covalent and metallic bonding in the boron intercalation superconductor MgB_2, Phys. Rev. B 64 (2001) 092503.

[10] I.I. Mazin, V.P. Antropov, Electronic structure, electron–phonon coupling, and multiband effects in MgB_2, Phys. C: Supercond. 385 (2003) 49–65.

[11] F. Bouquet, R.A. Fisher, N.E. Phillips, D.G. Hinks, J.D. Jorgensen, Specific heat of $Mg^{11}B_2$: Evidence for a second energy gap, Phys. Rev. Lett. 87 (2001) 047001.

[12] P. Szabó, P. Samuely, J. Kačmarčík, T. Klein, J. Marcus, D. Fruchart, S. Miraglia, C. Marcenat, A.G. M. Jansen, Evidence for two superconducting energy gaps in MgB_2 by point-contact spectroscopy, Phys. Rev. Lett. 87 (2001) 137005.

[13] H.J. Choi, D. Roundy, H. Sun, M.L. Cohen, S.G. Louie, The origin of the anomalous superconducting properties of MgB_2, Nature 418 (2002) 758-760.

[14] S. Souma, Y. Machida, T. Sato, T. Takahashi, H. Matsui, S. C. Wang, H. Ding, A. Kaminski, J. C. Campuzano, S. Sasaki, K. Kadowaki, The origin of multiple superconducting gaps in MgB_2, Nature 423 (2003) 65-67.

[15] E. Nishibori, M. Takata, M. Sakata, H. Tanaka, T. Muranaka, J. Akimitsu, Bonding Nature in MgB_2, J. Phys. Soc. Jpn. 70 (2001) 2252-2254.

[16] S.Y. Wu, P.H. Shih, J.-Y. Ji, T.-S. Chan, C.C. Yang, Direct observation of charge re-distribution in a MgB_2 superconductor, Supercond. Sci. Technol. 29 (2016) 045001.

[17] M. Maeda, J.H. Choi, J.C. Knott, J.H. Kim, G. Hahn, H. Kang, S. Hahn, S. Choi, Disorder anisotropy of layered structure in multi-band MgB_2 superconducting materials with high critical current performance, J. Alloys Compd. 934 (2023) 167873.

[18] A.A. Polyanskii, F. Kametani, D. Abraimov, A. Gurevich, A. Yamamoto, I. Pallecchi, M. Putti, C. Zhuang, T. Tan, X.X. Xi, Roles of intrinsic anisotropy and π-band pairbreaking effects on critical currents in tilted-*c*-axis MgB_2 films probed by magneto-optical and transport measurements, Phys. Rev. B 90 (2014) 214509.

[19] M. Maeda, D. Patel, H. Kumakura, G. Nishijima, A. Matsumoto, S. Kim, S. Choi, Influence of out-of-plane disorder formed by low-temperature sintering on carbohydrate-doped MgB_2 wire, Ceram. Int. 46 (2020) 21752-21756.

[20] A. Serquis, Y.T. Zhu, E.J. Peterson, J.Y. Coulter, D.E. Peterson, F.M. Mueller, Effect of lattice strain and defects on the superconductivity of MgB_2, Appl. Phys. Lett. 79 (2001) 4399-4401.

[21] S.K. Chen, K.A. Yates, M.G. Blamire, J.L. MacManus-Driscoll, Strong influence of boron precursor powder on the critical current density of MgB_2, Supercond. Sci. Technol. 18 (2005) 1473-1477.

[22] B.J. Senkowicz, R.J. Mungall, Y. Zhu, J. Jiang, P.M. Voyles, E.E. Hellstrom, D.C. Larbalestier, Nanoscale grains, high irreversibility field and large critical current density as a function of high-energy ball milling time in C-doped magnesium diboride, Supercond. Sci. Technol. 21 (2008) 035009.

[23] H.W. Li, T. Matsunaga, Y. Yan, H. Maekawa, M. Ishikiriyama, S.-I. Orimo, Nanostructure-induced hydrogenation of layered compound MgB_2, J. Alloys Compd. 505 (2010) 654-656.

[24] N. Varghese, K. Vinod, M.K. Chattopadhyay, S.B. Roy, U. Syamaprasad, Effect of combined addition of nano-SiC and nano-Ho_2O_3 on the in-field critical current density of MgB_2 superconductor, J. Appl. Phys. 107 (2010) 013907.

[25] M. Maeda, S. Choi, Effects of boron powder by hydrocarbon gas treatment on the structural and superconducting properties of in situ-processed MgB_2 polycrystalline materials, J. Alloys Compd. 787 (2019) 1265-1271.

[26] J.H. Choi, D.G. Lee, J.H. Jeon, E.J. Lee, M. Maeda, S. Choi, Customized MgB_2 Superconducting Wire Toward Practical Applications at Sam Dong in Korea, J. Supercond. Nov. Magn. 32 (2019) 1219-1223.

[27] J. H. Kim, X. Xu, M. S. A. Hossain, D. Q. Shi, Y. Zhao, X. L. Wang, S. X. Dou, S. Choi, T. Kiyoshi, Influence of disorder on the in-field J_c of MgB_2 wires using highly active pyrene, Appl. Phys. Lett. 92 (2008) 042506.

[28] K. Momma and F. Izumi, VESTA 3 for three-dimensional visualization of crystal, volumetric and morphology data, J. Appl. Crystallogr. 44 (2011) 1272-1276.

[29] F. Izumi, T. Ikeda, Three-Dimensional Visualization in Powder Diffraction, Solid State Phenom. 130 (2007) 15–20.

[30] D.L. Bish, S.A. Howard, Quantitative phase analysis using the Rietveld method, J. Appl. Crystallogr.

21 (1988) 86-91.

[31] R.J. Hill, C.J. Howard, Quantitative phase analysis from neutron powder diffraction data using the Rietveld method, J. Appl. Crystallogr. 20 (1987) 467-474.

[32] J.C. Taylor, C.E. Matulis, Absorption contrast effects in the quantitative XRD analysis of powders by full multiphase profile refinement, J. Appl. Crystallogr. 24 (1991) 14-17.

[33] G.W. Brindley, The effect of grain or particle size on x-ray reflections from mixed powders and alloys, considered in relation to the quantitative determination of crystalline substances by x-ray methods, Philos. Mag. 36 (1945) 347.

[34] G. Thorkildsen, H.B. Larsen, Absorption and Weighted Path Lengths in Cylinders and Spheres, Acta. Crystallogr. Sect. A 54 (1998) 186-190.

[35] S. Choi, D. Patel, J.H. Kim, H. Kumakura, A. Matsumoto, G. Nishijima, S.H. Kim, J. Joo, M. Maeda, Evaluation and control of residual amorphous phases in carbon-doped MgB_2 superconductors, J. Alloys Compd. 864 (2021) 158867.

[36] T. de Keijser, E.J. Mittemeijer, H.C.F. Rozendaal, The Determination of Crystallite-Size and Lattice-Strain Parameters in Conjunction with the Profile-Refinement Method for the Determination of Crystal Structures, J. Appl. Cryst. 16 (1983) 309-316.

[37] G.K. Wertheim, M.A. Butler, K.W. West, D.N.E. Buchanan, Determination of the Gaussian and Lorentzian content of experimental line shapes, Rev. Sci. Instrum. 45 (1974) 1369-1371.

[38] P. Scherrer, Bestimmung der Größe und der inneren Struktur von Kolloidteilchen mittels Röntgenstrahlen, Nachr. Ges. Wiss. Göttingen, Math.-Phys. Kl. 1918 (1918) 98-100 http://eudml.org/doc/59018

[39] J.C. Loudon, S. Yazdi, T. Kasama, N.D. Zhigadlo, J. Karpinski, Measurement of the penetration depth and coherence length of MgB_2 in all directions using transmission electron microscopy, Phys. Rev. B 91 (2015) 054505.

[40] A. Brinkman, A.A. Golubov, H. Rogalla, O.V. Dolgov, J. Kortus, Y. Kong, O. Jepsen, O.K. Andersen, Multiband model for tunneling in MgB_2 junctions, Phys. Rev. B 65 (2002) 180517.

[41] M. Zehetmayer, M. Eisterer, J. Jun, S.M. Kazakov, J. Karpinski, A. Wisniewski, H.W. Weber, Mixed-state properties of superconducting MgB_2 single crystals, Phys. Rev. B 66 (2002) 052505.

[42] M.R. Eskildsen, M. Kugler, S. Tanaka, J. Jun, S.M. Kazakov, J. Karpinski, Ø. Fischer, Vortex Imaging in the π Band of Magnesium Diboride, Phys. Rev. Lett. 89 (2002) 187003.

[43] J.H. Kim, S. Oh, Y.U. Heo, S. Hata, H. Kumakura, A. Matsumoto, M. Mitsuhara, S. Choi, Y. Shimada, M. Maeda, J.L. MacManus-Driscoll, S.X. Dou, Microscopic role of carbon on MgB_2 wire for critical current density comparable to NbTi, NPG Asia Mater. 4 (2012) E3.

[44] M. Maeda, Y.-U. Heo, J.H. Choi, D. Patel, S.-H. Kim, S. Hahn, J.H. Kim, S. Choi, Interfacial reaction and side effect of MgB_2 superconducting material through low-rotation mechanical milling, Ceram. Int. 48 (2022) 6539-6548.

[45] M. Maeda, D. Uchiyama, M.S.A. Hossain, Z. Ma, M. Shahabuddin, J.H. Kim, Control of core structure in MgB2 wire through tailoring boron powder, J. Alloys Compd. 636 (2015) 29–33.

Supporting Information

Evaluation of in-plane and out-of-plane crystallinities with residual amorphous phases for MgB_2 superconductor

Minoru Maeda[a], Jun Hyuk Choi[b], Dong Gun Lee[b], Akiyoshi Matsumoto[c], Gen Nishijima[c], Zhenan Jiang[d], Nicholas M. Strickland[d], Jung Ho Kim[e], Seyong Choi[a]

[a] *Department of Electrical Engineering and Kangwon High Magnetic Field Center, Institute of Quantum Convergence Technology, Kangwon National University, Gangwon 24341, Republic of Korea*

[b] *Sam Dong Co., Ltd., Daejeon 34027, Republic of Korea*

[c] *Superconducting System Group, Research Center for Energy and Environmental Materials (GREEN), National Institute for Materials Science (NIMS), Sengen, Tsukuba, Ibaraki 305-0047, Japan*

[d] *Paihau-Robinson Research Institute, Victoria University of Wellington, Wellington, Lower Hutt 5011, New Zealand*

[e] *Institute for Superconducting and Electronic Materials, Faculty of Engineering and Information Sciences, University of Wollongong, Squires Way, Innovation Campus, North Wollongong, New South Wales 2500, Australia*

*Corresponding authors: jhk@uow.edu.au (J.H. Kim); syc@kangwon.ac.kr (S. Choi)

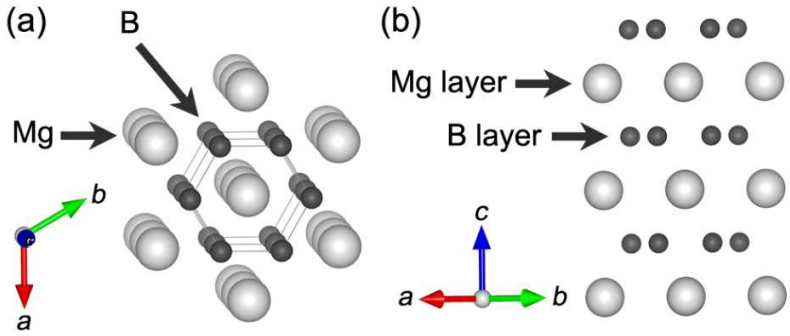

Supplementary Fig. S1. (a, b) Schematic illustrations of the periodic structure in MgB_2 crystals for (a) overhead and (b) lateral views. These illustrations were drawn using the VESTA program [28]. The light gray and black spheres denote Mg and B atoms, respectively. The red, green, and blue arrows denote the *a*-, *b*-, and *c*-axis directions, respectively. Mg and B layers are stacked alternately along the *c*-axis direction in the crystal structure of MgB_2.

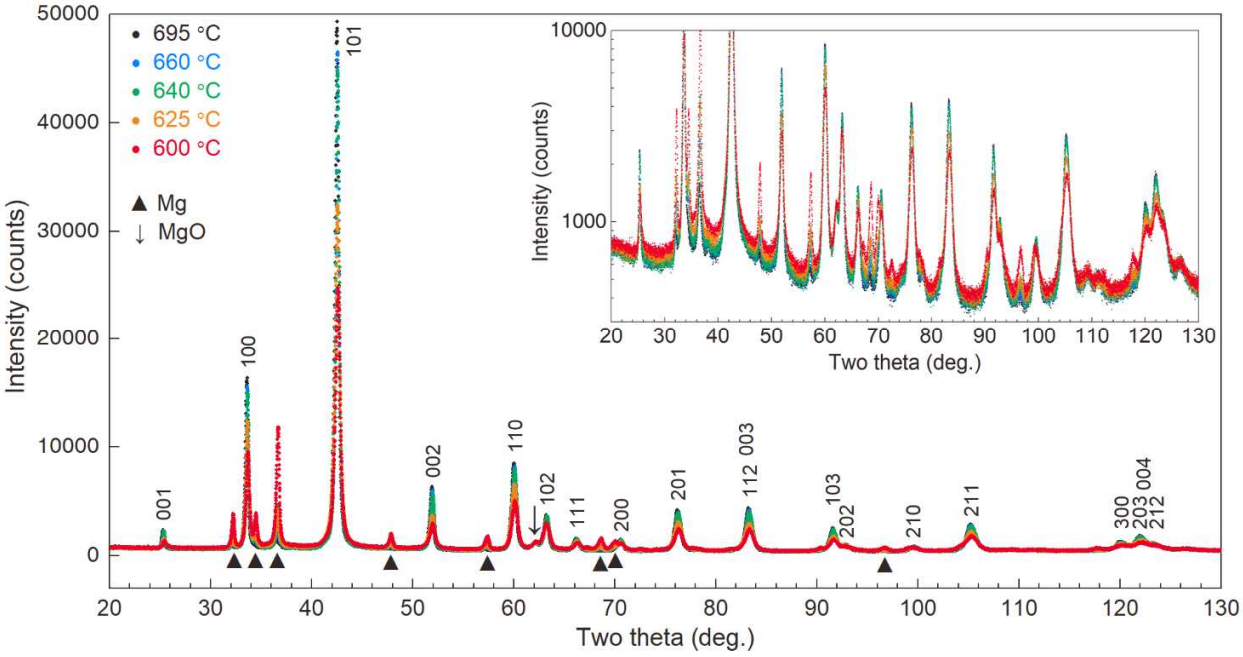

Supplementary Fig. S2. XRD patterns of the powder samples sintered at 600 ºC, 625 ºC, 640 ºC, 660 ºC, and 695 ºC for 8 hours. The XRD measurements were performed without the addition of the Si powder, unlike the case of Fig. 1. The lines of black, blue, green, orange, and red plots are the observed XRD patterns. The Miller indices (*hkl* = 001, 100, 101, 002, 110, 102, 111, 200, 201, 003, 112, 103, 202, 210, 211, 300, 203, 004, and 212) denote peaks of the MgB_2 phase. The upright triangles and the arrow denote the Mg phase and the MgO phase, respectively. A semi-log plot of the intensities for the XRD patterns is also inserted in the figure. The inserted figure is used here to clarify the background behaviors in the XRD patterns. It was found that the background intensity is elevated with a decrease in the sintering temperature. This phenomenon reflects an increase in the content of amorphous phases that cannot be detected as distinct peaks in the XRD patterns. In addition, lowering the sintering temperature strongly reduced the peak intensities of the MgB_2 phase and increased the peak intensities of the Mg phase. This means an increase in the content of unreacted Mg. The increased presence of the unreacted phase may lead to a rise in the content of amorphous B phase that comes from amorphous B powder used as a starting material. The increase in the amorphous phase can contribute to the elevation of the background intensity.

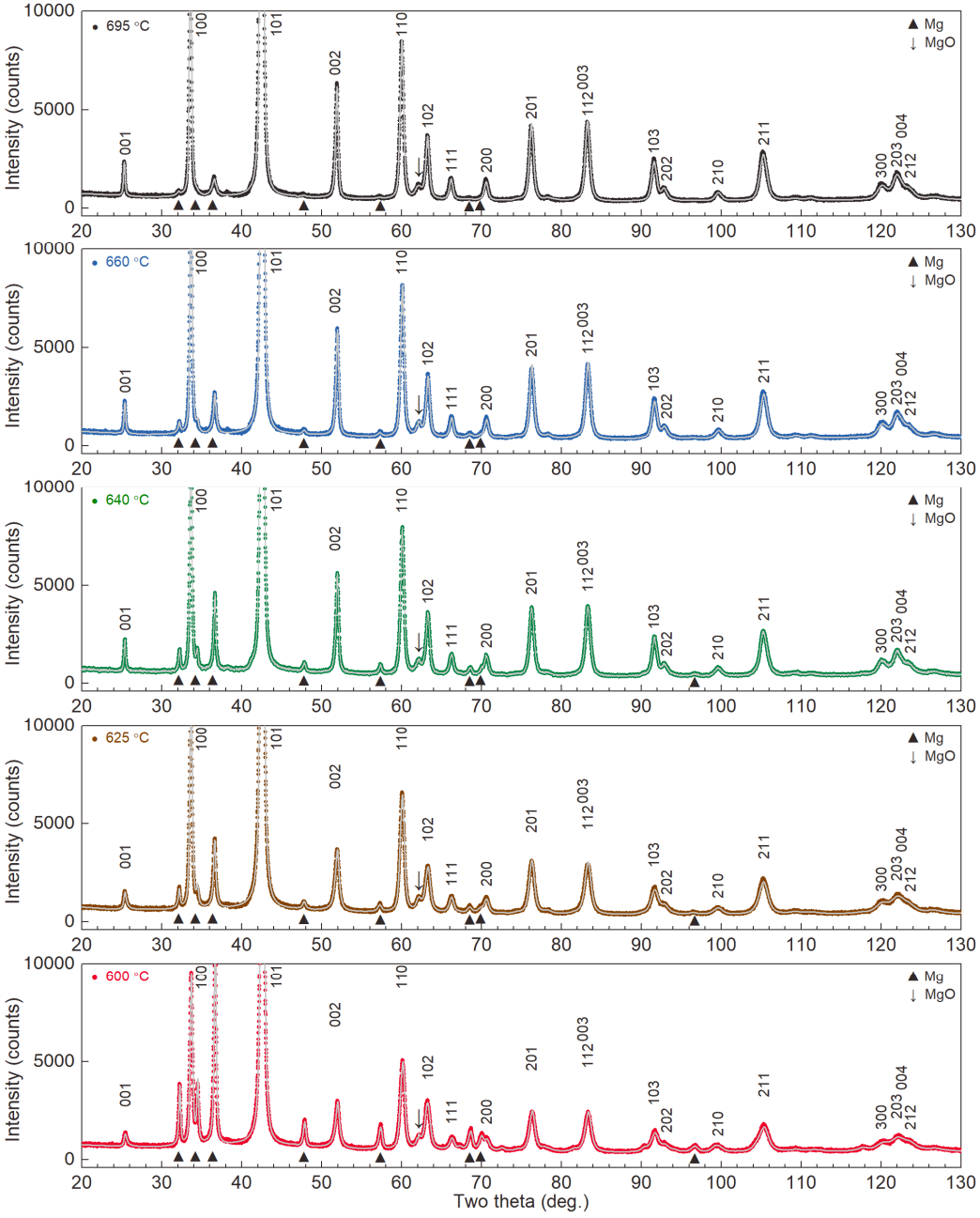

Supplementary Fig. S3. The calculated patterns obtained by Rietveld refinement for the XRD peaks of the powder samples sintered at 600 ºC, 625 ºC, 640 ºC, 660 ºC, and 695 ºC for 8 hours. The lines of black, blue, green, brown, and red plots are the observed XRD patterns, which are the same as those shown in Supplementary Fig. S2. The thin gray lines, overlapping the black, blue, green, brown, and red lines, are the calculated patterns obtained by Rietveld refinement. The Miller indices (*hkl* = 001, 100, 101, 002, 110, 102, 111, 200, 201, 003, 112, 103, 202, 210, 211, 300, 203, 004, and 212) denote peaks of the MgB_2 phase. The upright triangles and the arrow denote the Mg phase and the MgO phase, respectively.

Supplementary Table S1. The estimated values of 2θ, β_{obs}, $\beta_{L,obs}$, $\beta_{G,obs}$, $\beta_{L,inst}$, $\beta_{G,inst}$, $\beta_{L,sample}$, $\beta_{G,sample}$, and β_{sample} for the in-plane and the out-of-plane peaks in the XRD pattern in the case of the powder sample sintered at 600 ºC for 8 hours. Details about the definition and calculation of these values are explained in the manuscript. In this table, *h*, *k*, and *l* are Miller indices for the diffraction peaks of the MgB_2 phase. Note that two angle units (deg. and rad) are used in this table.

h	*k*	*l*	2θ (deg.)	β_{obs} (deg.)	$\beta_{L,obs}$ (deg).	$\beta_{G,obs}$ (deg.)	$\beta_{L,inst.}$ (rad)	$\beta_{G,inst}$ (rad)	$\beta_{L,sample}$ (rad)	$\beta_{G,sample}$ (rad)	β_{sample} (deg.)
0	0	1	25.27	0.59	0.51	0.19	0.00113	0.00104	0.00774	0.00320	0.53
1	0	0	33.56	0.50	0.38	0.21	0.00122	0.00100	0.00540	0.00361	0.44
0	0	2	51.88	0.83	0.81	0.06	0.00146	0.00093	0.01270	0.00053	0.73
1	1	0	60.01	0.84	0.63	0.38	0.00158	0.00090	0.00937	0.00650	0.78
2	0	0	70.54	0.99	0.88	0.29	0.00176	0.00087	0.01351	0.00497	0.90
0	0	3	82.02	1.22	1.04	0.41	0.00200	0.00084	0.01609	0.00715	1.13
2	1	0	99.62	1.59	1.33	0.57	0.00250	0.00079	0.02066	0.00990	1.49
3	0	0	120.03	2.29	1.85	0.89	0.00350	0.00065	0.02876	0.01544	2.16
0	0	4	122.06	2.39	1.97	0.87	0.00365	0.00062	0.03078	0.01522	2.24

Supplementary Table S2. The estimated values of 2θ, β_{obs}, $\beta_{L,obs}$, $\beta_{G,obs}$, $\beta_{L,inst}$, $\beta_{G,inst}$, $\beta_{L,sample}$, $\beta_{G,sample}$, and β_{sample} for the in-plane and the out-of-plane peaks in the XRD pattern in the case of the powder sample sintered at 625 ºC for 8 hours. Details about the definition and calculation of these values are explained in the manuscript. In this table, *h*, *k*, and *l* are Miller indices for the diffraction peaks of the MgB_2 phase. Note that two angle units (deg. and rad) are used in this table.

h	*k*	*l*	2θ (deg.)	β_{obs} (deg.)	$\beta_{L,obs}$ (deg).	$\beta_{G,obs}$ (deg.)	$\beta_{L,inst.}$ (rad)	$\beta_{G,inst}$ (rad)	$\beta_{L,sample}$ (rad)	$\beta_{G,sample}$ (rad)	β_{sample} (deg.)
0	0	1	25.27	0.57	0.54	0.10	0.00113	0.00104	0.00828	0.00148	0.49
1	0	0	33.56	0.49	0.38	0.20	0.00122	0.00100	0.00537	0.00337	0.43
0	0	2	51.89	0.81	0.77	0.15	0.00146	0.00093	0.01191	0.00246	0.72
1	1	0	60.00	0.81	0.61	0.35	0.00158	0.00090	0.00909	0.00605	0.74
2	0	0	70.53	0.95	0.84	0.28	0.00176	0.00087	0.01297	0.00485	0.87
0	0	3	82.04	1.25	1.07	0.41	0.00200	0.00084	0.01663	0.00714	1.16
2	1	0	99.60	1.55	1.30	0.54	0.00250	0.00079	0.02028	0.00935	1.45
3	0	0	120.00	2.20	1.75	0.88	0.00350	0.00065	0.02710	0.01528	2.07
0	0	4	122.10	2.29	1.76	0.98	0.00365	0.00062	0.02703	0.01701	2.15

Supplementary Table S3. The estimated values of 2θ, β_{obs}, $\beta_{L,obs}$, $\beta_{G,obs}$, $\beta_{L,inst}$, $\beta_{G,inst}$, $\beta_{L,sample}$, $\beta_{G,sample}$, and β_{sample} for the in-plane and the out-of-plane peaks in the XRD pattern in the case of the powder sample sintered at 640 ºC for 8 hours. Details about the definition and calculation of these values are explained in the manuscript. In this table, *h*, *k*, and *l* are Miller indices for the diffraction peaks of the MgB_2 phase. Note that two angle units (deg. and rad) are used in this table.

h	*k*	*l*	2θ (deg.)	β_{obs} (deg.)	$\beta_{L,obs}$ (deg).	$\beta_{G,obs}$ (deg.)	$\beta_{L,inst.}$ (rad)	$\beta_{G,inst}$ (rad)	$\beta_{L,sample}$ (rad)	$\beta_{G,sample}$ (rad)	β_{sample} (deg.)
0	0	1	25.26	0.33	0.28	0.12	0.00113	0.00104	0.00377	0.00174	0.27
1	0	0	33.56	0.39	0.32	0.15	0.00122	0.00100	0.00433	0.00242	0.33
0	0	2	51.87	0.52	0.45	0.16	0.00146	0.00093	0.00647	0.00254	0.44
1	1	0	60.00	0.66	0.54	0.25	0.00158	0.00090	0.00778	0.00425	0.59
2	0	0	70.53	0.74	0.64	0.24	0.00176	0.00087	0.00942	0.00414	0.66
0	0	3	82.00	0.82	0.70	0.28	0.00200	0.00084	0.01015	0.00476	0.73
2	1	0	99.59	1.22	1.02	0.43	0.00250	0.00079	0.01536	0.00743	1.11
3	0	0	120.00	1.74	1.38	0.69	0.00350	0.00065	0.02058	0.01206	1.59
0	0	4	122.04	1.47	1.12	0.63	0.00364	0.00062	0.01598	0.01093	1.32

Supplementary Table S4. The estimated values of 2θ, β_{obs}, $\beta_{L,obs}$, $\beta_{G,obs}$, $\beta_{L,inst}$, $\beta_{G,inst}$, $\beta_{L,sample}$, $\beta_{G,sample}$, and β_{sample} for the in-plane and the out-of-plane peaks in the XRD pattern in the case of the powder sample sintered at 660 ºC for 8 hours. Details about the definition and calculation of these values are explained in the manuscript. In this table, *h*, *k*, and *l* are Miller indices for the diffraction peaks of the MgB_2 phase. Note that two angle units (deg. and rad) are used in this table.

h	*k*	*l*	2θ (deg.)	β_{obs} (deg.)	$\beta_{L,obs}$ (deg).	$\beta_{G,obs}$ (deg.)	$\beta_{L,inst.}$ (rad)	$\beta_{G,inst}$ (rad)	$\beta_{L,sample}$ (rad)	$\beta_{G,sample}$ (rad)	β_{sample} (deg.)
0	0	1	25.26	0.34	0.32	0.06	0.00113	0.00104	0.00442	0.00020	0.25
1	0	0	33.56	0.39	0.33	0.14	0.00122	0.00100	0.00446	0.00227	0.33
0	0	2	51.87	0.51	0.45	0.16	0.00146	0.00093	0.00638	0.00254	0.44
1	1	0	60.00	0.66	0.55	0.23	0.00158	0.00090	0.00807	0.00393	0.59
2	0	0	70.53	0.73	0.64	0.23	0.00176	0.00087	0.00944	0.00386	0.65
0	0	3	82.00	0.82	0.69	0.28	0.00200	0.00084	0.01009	0.00483	0.73
2	1	0	99.60	1.19	1.00	0.42	0.00250	0.00079	0.01501	0.00724	1.09
3	0	0	120.01	1.69	1.31	0.70	0.00350	0.00065	0.01943	0.01214	1.54
0	0	4	122.03	1.43	1.10	0.61	0.00364	0.00062	0.01558	0.01057	1.28

Supplementary Table S5. The estimated values of 2θ, β_{obs}, $\beta_{L,obs}$, $\beta_{G,obs}$, $\beta_{L,inst}$, $\beta_{G,inst}$, $\beta_{L,sample}$, $\beta_{G,sample}$, and β_{sample} for the in-plane and the out-of-plane peaks in the XRD pattern in the case of the powder sample sintered at 695 ºC for 8 hours. Details about the definition and calculation of these values are explained in the manuscript. In this table, *h*, *k*, and *l* are Miller indices for the diffraction peaks of the MgB_2 phase. Note that two angle units (deg. and rad) are used in this table.

h	*k*	*l*	2θ (deg.)	β_{obs} (deg.)	$\beta_{L,obs}$ (deg).	$\beta_{G,obs}$ (deg.)	$\beta_{L,inst.}$ (rad)	$\beta_{G,inst}$ (rad)	$\beta_{L,sample}$ (rad)	$\beta_{G,sample}$ (rad)	β_{sample} (deg.)
0	0	1	25.27	0.33	0.29	0.09	0.00113	0.00104	0.00397	0.00126	0.26
1	0	0	33.56	0.39	0.32	0.14	0.00122	0.00100	0.00434	0.00229	0.32
0	0	2	51.88	0.50	0.42	0.18	0.00146	0.00093	0.00588	0.00296	0.43
1	1	0	60.01	0.64	0.52	0.25	0.00158	0.00090	0.00752	0.00421	0.57
2	0	0	70.54	0.73	0.63	0.23	0.00176	0.00087	0.00922	0.00392	0.64
0	0	3	82.01	0.80	0.67	0.28	0.00200	0.00084	0.00965	0.00482	0.71
2	1	0	99.61	1.17	0.96	0.44	0.00250	0.00079	0.01424	0.00756	1.06
3	0	0	120.02	1.64	1.21	0.74	0.00350	0.00065	0.01759	0.01290	1.49
0	0	4	122.05	1.40	1.06	0.61	0.00364	0.00062	0.01480	0.01060	1.24

Supplementary Table S6. The estimated values of the in-plane and out-of-plane coherence lengths ξ_{σ}^{ab}, ξ_{π}^{ab}, and ξ_{π}^{c}. These values are estimated from experimental results in the literature [39,41,42].

$\xi_{crystal}^{ab}\left(=\xi_{\sigma}^{ab}\right)$ (nm) [1]	ξ_{π}^{ab} (nm) [2]	ξ_{π}^{c} (nm) [3]
~10.2	~49.6	35 ± 10

[1] The value was estimated from the upper critical field of single crystals [41]

[2] The value was estimated through imaging of the flux vortices by scanning tunnelling spectroscopy, especially for the π bands [42]. The tunnelling direction and the magnetic field were parallel to the *c* axis. The tip scan direction was parallel to the *ab* plane, so that the in-plane coherence length ξ_{π}^{ab} could be evaluated.

[3] The value was estimated through imaging of the flux vortices by transmission electron microscopy, especially for the π bands [39].

Supplementary Table S7. The calculated values of the in-plane and out-of-plane coherence lengths $\xi_{0,\sigma}^{ab}$, $\xi_{0,\pi}^{ab}$, and $\xi_{0,\pi}^{c}$. These values were obtained from the Bardeen–Cooper–Schrieffer (BCS) relation $\xi_0 = \hbar v_{\mathrm{F}}/\pi\Delta(0)$ by Brinkman's calculation [17,40]. Here, ξ_0 v_{F}, and $\Delta(0)$ are the clean-limit coherence length, the average Fermi velocity, and the superconducting gap, respectively.

$\xi_{0,\sigma}^{ab}$ (nm)	$\xi_{0,\pi}^{ab}$ (nm)	$\xi_{0,\pi}^{c}$ (nm)
~13	~42	~48